crystals

MDPI

Article

Synthesis, Crystal and Electronic Structures, Nonlinear Optical Properties, and Magnetic Properties of Two Thiophosphates: $KInP_2S_7$ and $KCrP_2S_7$

Craig Cropek [1], Vivian Nguyen [1], Santosh Karki Chhetri [2], Jin Hu [2,3], Shengping Guo [4] and Jian Wang [1,*]

[1] Department of Chemistry and Biochemistry, Wichita State University, Wichita, KS 67260, USA
[2] Department of Physics, University of Arkansas, Fayetteville, AR 72701, USA
[3] Materials Science and Engineering Program, Institute for Nanoscience and Engineering, University of Arkansas, Fayetteville, AR 72701, USA
[4] School of Chemistry and Chemical Engineering, Yangzhou University, Yangzhou 225002, China
* Correspondence: jian.wang@wichita.edu

Abstract: Two thiophosphates, $KInP_2S_7$ and $KCrP_2S_7$, were structurally characterized without investigating any optical properties. Herein in this work, $KInP_2S_7$ and $KCrP_2S_7$ were revisited to investigate their optical and magnetic properties, respectively. Pure polycrystalline samples and crystals of $KInP_2S_7$ and $KCrP_2S_7$ were grown by high temperature solid state reactions, where mm-sized crystals of $KCrP_2S_7$ were collected. $KCrP_2S_7$ is isostructural to $KInP_2S_7$, which features a layered structure. $KInP_2S_7$ and $KCrP_2S_7$ possess close relationship to the layered thiophosphate $M_2P_2S_6$ (M = Fe, Co, Zn, etc.). The bonding pictures of $KInP_2S_7$ were studied using the electron localization function (ELF) coupled with crystal orbital Hamilton population (COHP) calculations. The intrinsically distorted [PS_4] tetrahedra and [InS_6] octahedra are made by strong covalent P-S interactions and ionic In-S interactions, respectively. Electronic structure analysis confirmed that the optical properties of $KInP_2S_7$ are mainly contributed to by [PS_4] tetrahedra together with small amounts of the contributions coming from [InS_6] octahedra. Magnetic measurement on mm-sized crystals of $KCrP_2S_7$ verified that there is an antiferromagnetic transition around 21 K, and the Cr atoms are trivalent. $KInP_2S_7$ is predicated to be an indirect bandgap semiconductor of 2.38 eV, which is confirmed by the UV-Vis measurement of 2.4(1) eV. $KInP_2S_7$ is not a type-I phase-matching material and exhibits moderate second harmonic generation (SHG) response (0.51 × $AgGaS_2$, sample of particle size of 100 μm). The laser damage threshold (LDT) of $KInP_2S_7$ is very high of 5.2 × $AgGaS_2$. Bandgap engineering were undergone to enhance the SHG response of $KInP_2S_7$.

Keywords: solid state synthesis; crystal growth; antiferromagnetic transition; nonlinear

check for updates

Citation: Cropek, C.; Nguyen, V.; Chhetri, S.K.; Hu, J.; Guo, S.; Wang, J. Synthesis, Crystal and Electronic Structures, Nonlinear Optical Properties, and Magnetic Properties of Two Thiophosphates: $KInP_2S_7$ and $KCrP_2S_7$. *Crystals* **2022**, *12*, 1505. https://doi.org/10.3390/cryst12111505

Academic Editors: Mingjun Xia and Lijuan Liu

Received: 22 September 2022
Accepted: 19 October 2022
Published: 22 October 2022

1. Introduction

Thiophosphates, which are constructed by phosphorus and sulfur atoms, have attracted growing interests due to important applications such as nonlinear optical applications [1–16], ion conductors [17–26], hydrogen evolution [27,28], and photocurrent response [29]. The chemical flexibility of thiophosphates accounts for their fruitful applications. The chemical flexibility originates from flexible crystal structures spanning from three dimensional (3D) frameworks [25,30], two-dimensional layered structures [31], and one-dimensional chain structures [32]. Phosphorus and sulfur elements share many similar properties such as low melting points, high volatile nature and easily form homoatomic bonds, etc. There exist significant different properties between phosphorus and sulfur, for example, electron configuration and electronegativity. The phosphorus atoms are surrounded by four sulfur atoms forming a tetrahedron, which are interconnected via the sharing of apex sulfur atoms, homoatomic P-P bonds, or homoatomic S-S bonds to form various [P_xS_y] motifs [1–16]. The flexible [P_xS_y] motifs, interacting with metals, generate the flexible structures of thiophosphates [1–16].

An acentric thiophosphate group, $AIIIP_2S_7$ (A = K, Rb, Cs; III = V, Cr, In) [33–37] has attracted our attention due to their interesting structures and the presence of both transition metals and main group elements within one system. The trivalent transition metals V^{3+} and Cr^{3+} possess unpaired *d*-electrons, which introduces magnetic properties into the $AIIIP_2S_7$ family. The crystal structures of $AIIIP_2S_7$ were studied by few groups. To the best of our knowledge, there were no systemic study of synthesis, electronic structure, bonding pictures, and nonlinear optical properties of the $AIIIP_2S_7$ family, reported. A previous study found interesting magnetic properties of $KV_{1-x}Cr_xP_2S_7$ (X = 0, 0.75, 1), where KBr was utilized as a transport agent and a source of K [37]. In this work, we selected $KInP_2S_7$ and $KCrP_2S_7$ from the $AIIIP_2S_7$ family as our study objectives. A systematic study of synthesis, electronic structure, bonding pictures, and nonlinear optical properties of $KInP_2S_7$ are presented in this work. A detailed magnetic study of $KCrP_2S_7$, based on crystals grown from solid state reactions, were carried out, which resulted in the findings of the presence of an antiferromagnetic transition around 21 K. $KInP_2S_7$ was found as an indirect semiconductor of a bandgap of 2.38 eV and 2.4(1) eV, supported by tight-binding calculations and UV-Vis measurements, respectively. The Nonlinear optical properties of $KInP_2S_7$ were also measured in this work. The electronic structure and bonding picture studies of $KInP_2S_7$ were also studied in this work.

2. Materials and Methods

2.1. Synthesis

All starting materials were used as received without further processing, except for the cutting of solid metals: Potassium metal (Thermo Fisher Scientific, Waltham, MA, USA, 99.5%, indium shot metal basis (Thermo Fisher Scientific, MA, USA, 99.9%), chromium powder (Sigma-Aldrich, St. Louis, MO, USA, 99.5%), phosphorus powder (Alfa Aesar, Ward Hill, MA, USA, 99.5%), sulfur powder (Thermo Fisher Scientific, MA, USA, 99.5%). These reactants were stored in an argon-filled glovebox. Moisture and oxygen levels are maintained below 0.5 ppm. All preparations were done in a glovebox and sealed under a vacuum. All quartz ampoules were sealed under 100 mTorr.

2.1.1. $KCrP_2S_7$ Single Crystal Growth

0.4000 g of reactants were loaded into a 9 mm inner-diameter carbonized silica ampoule at a stoichiometric ratio of K:Cr:P:S = 1:1:2:7. Potassium was rolled in pre-weighed chromium powder before adding to the ampoule. After sealing, these reactants were loaded into a programmable muffle furnace. The reactants were heated from room temperature to 125 °C in 10 h, dwelled for 10 h, heated up to 700 °C in 10 h, dwelled for 96 h, and then cooled to room temperature in 24 h. High quality large black needles were obtained. Formation of $KCrP_2S_7$ was verified using powder X-ray diffraction (*vide infra*).

2.1.2. $KInP_2S_7$

0.5000 g total of reactants were loaded into a 9 mm inner-diameter carbonized silica ampoule at a stoichiometric ratio of K:In:P_2S_5:S = 1.2:1:1:2, and in that order. P_2S_5 was grown as a single phase via heating stoichiometric ratio of P and S at 350 °C for 24 h. Ampoules were capped using parafilm and then pumped out of the glovebox for sealing. The ampules were sealed to an inner-ampoule length of about 8.3 cm. After sealing the ampoules, they were placed vertically in a programmable muffle furnace and separated, by about 2.5 cm, in individual ampoule holders held in a homemade quartz holder setup. The reactants were heated from room temperature to 125 °C in 10 h, dwelled for 10 h, heated up to 650 °C in 10 h, dwelled for 96 h, ramped down for 24 h to room temperature. A second annealing process was necessary to improve the phase purity. Amber single crystals and an amber colored mass was obtained. Formation of $KInP_2S_7$ was verified using powder X-ray diffraction (Figure S1). $KInP_2S_7$ and $KCrP_2S_7$ were stable in dry air for a few weeks. Within a high moisture environment, $KInP_2S_7$ and $KCrP_2S_7$ would slowly decompose into amorphous products.

2.2. Powder X-ray Diffraction

Powder X-ray diffraction data were collected at room temperature using a Rigaku Mini Flex VI diffractometer with Cu-Kα radiation (λ = 1.5406 Å) in the range 2θ = 10°–80°, at a scan step of 0.04° with ten seconds exposure time.

2.3. UV-Vis Measurements

Diffuse-reflectance spectra were recorded at room temperature by a PERSEE-T8DCS UV-Vis spectrophotometer equipped with an integration sphere in the wavelength range of 230−850 nm. The reflectance data, R were recorded and converted to the Kubelka-Munk function, $f(R) = (1 - R)^2(2R)^{-1}$. The Tauc plots, $(KM \times E)^2$ and $(KM \times E)^{1/2}$, were applied to estimate direct and indirect bandgaps, respectively.

2.4. Second Harmonic Measurements

Using the Kurtz and Perry method [38], powder SHG responses of $KInP_2S_7$ compound were investigated by a Q-switch laser (2.09 μm, 3 Hz, 50 ns) with various particle sizes, including 38.5–54, 54–88, 88–105, 105–150, and 150–200 μm. Homemade $AgGaS_2$ was selected as the reference. The lab-synthesized $AgGaS_2$ crystals were ground to the same size range as $KInP_2S_7$. The LDTs of the title compounds were evaluated on powder samples (150−200 μm) with a pulsed YAG laser (1.06 μm, 10 ns, 10 Hz). The judgment criterion is as follows: with increasing laser energy, the color change of the powder sample is constantly observed by an optical microscope to determine the damage threshold. To adjust different laser beams, an optical concave lens is added to the laser path. The damaged spot is measured by the scale of the optical microscope.

2.5. TB-LMTO-ASA Calculations

The density of states (DOS), partial density of states (PDOS), band structure, crystal orbital Hamilton population (COHP), and electron localization function (ELF) of $KInP_2S_7$ are calculated using the tight binding-linear muffin tin orbitals-atomic sphere approximation (TB-LMTO-ASA) program [39,40]. The Barth-Hedin exchange potential was employed for the LDA calculations [39]. The radial scalar-relativistic Dirac equation was solved to obtain the partial waves. The basis set used contained K (4*s*), In (5*s*, 5*p*, 5*d*) P (3s, 3p) and S (3*s*, 3*p*) orbitals, and was employed for a self-consistent calculation, with downfolded functions of K (*4p, 3d*), In (*4f, 5d*), P (*3d*) and S (3*d*). The density of states and band structures were calculated after converging the total energy on a dense k-mesh of $KInP_2S_7$ (16 × 16 × 16 points with 2064 irreducible k-points).

2.6. Magnetic Properties Measurements

Temperature dependence of magnetic susceptibility and isothermal magnetization measurements were performed by using the ACMSII option of a physical properties measurement system (PPMS).

3. Results and Discussion

3.1. Synthesis and Crystal Growth

To reduce the chance of incorporating foreign elements, a high temperature solid state synthetic method was preferred in this study. Due to the high reactive nature of potassium metals, the bottom of silica tubes was protected by amorphous carbon. Large mm-sized single crystals of $KCrP_2S_7$ were collected as shown in Figure 1 inset. The powder X-ray diffraction results confirmed the single-phase nature of $KCrP_2S_7$ as shown in Figure 1. The large $KCrP_2S_7$ crystals were manually selected and cleaved for magnetic measurements (*vide infra*). Pure samples of $KInP_2S_7$ were also collected after a high temperature solid state reaction (Figure S1). The crystals of $KInP_2S_7$ did not grow as large as the $KCrP_2S_7$. The final products of $KInP_2S_7$ are a mixture of $KInP_2S_7$ small crystals and polycrystalline powder chunks.

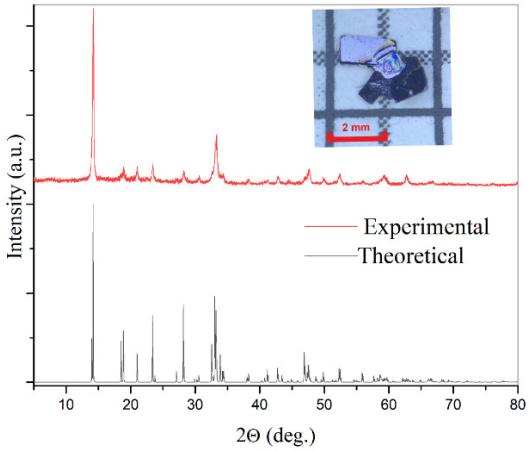

Figure 1. Powder X-ray diffraction results of $KCrP_2S_7$, the insert shows the optical microscope photo of selected $KCrP_2S_7$ crystals. The crystals were manually cut and selected for properties measurements.

3.2. Crystal Structures

$KCrP_2S_7$ is isostructural to $KInP_2S_7$, which both crystallizes in the $LiFeAs_2O_7$ structure type and the acentric *C2* (no.5) space group [35]. The acentric nature of $KInP_2S_7$ is confirmed by SHG measurements (*vide infra*). To simplify the discussion, $KInP_2S_7$ is selected to present the structural chemistry. The structure of $KInP_2S_7$ is summarized in Figure 2b,d. $KInP_2S_7$ possesses clear layered features, which is constructed by two-dimensional (2D) $[InP_2S_7]^-$slabs sandwiched by K^+ cations. The detailed view of 2D $[InP_2S_7]^-$ slab is shown in Figure 2d. The 2D $[InP_2S_7]^-$ slab is built by $[InS_6]$ octahedra and $[P_2S_7]$ units. The $[InS_6]$ octahedra are interconnected to the $[P_2S_7]$ units via sharing edges and vertices. The $[P_2S_7]$ units are made by two $[PS_4]$ tetrahedra via sharing one apex sulfur atom. Each In atom is in the center of a distorted octahedron with the In-S distance falling into the range of 2.581–2.698 Å [35]. The P-S distances within $[PS_4]$ tetrahedra are 2.005–2.137 Å, which are comparable to many thiophosphates such as α-$Ba_2P_2S_6$ (1.99(2)–2.04(2) Å) [15], β-$Ba_2P_2S_6$(2.017(2)–2.028(2) Å) [15], $Pb_2P_2S_6$(2.011(19)–2.040(18) Å) [15], $K_2BaP_2S_6$ (1.958(17)–2.066(15) Å) [41], $KSbP_2S_6$ (1.962(1)–2.077(1) Å) [42], $KBiP_2S_6$ (1.961(3)–2.059(3) Å) [43], $Pb_3P_2S_8$ (2.031–2.065 Å) [44], etc.

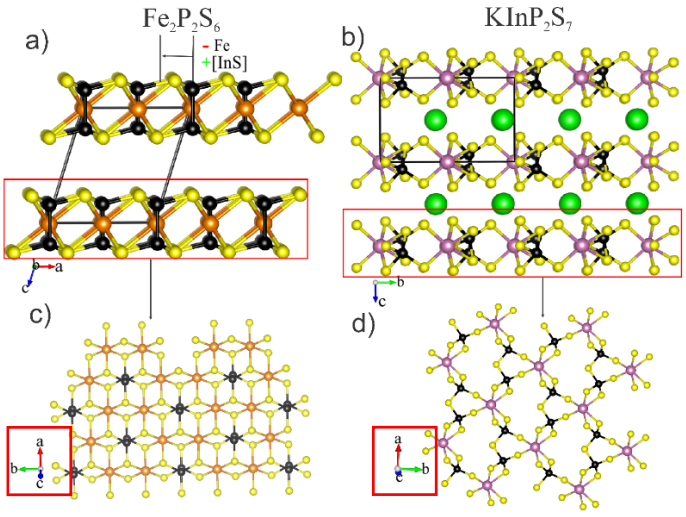

Figure 2. (**a**) Ball-stick structure of $Fe_2P_2S_6$ viewed along [010] direction, (**b**) ball-stick structure of $KInP_2S_7$ viewed along [100] direction, (**c**) a detailed view of $[FeP_2S_3]$ layers within $Fe_2P_2S_6$ viewed along [101] direction, (**d**) a detailed view of $[InP_2S_7]^-$ layer within $KInP_2S_7$ viewed along [101] direction. Fe: orange, P: black, S: yellow, K: green, In: pink.

One interesting point here would be the structure relationship between $KInP_2S_7$ and $M_2P_2S_6$ (M = Mg, Mn, Fe, Co, Ni, Zn, Cd, Pb, Sn or mixed occupancy of two metals) systems as shown in Figure 2 [31,45–54]. The $M_2P_2S_6$ system has emerged as an important system due to their 2D layered crystal structure coupled with highly tunable chemical properties via mixing various metals within the crystal lattice [31,45–54]. $KInP_2S_7$ shows quasi-layered features as shown in Figure 2b. Using $Fe_2P_2S_6$ as an example to present the structure of the $M_2P_2S_6$ system, which is shown in Figure 2a,c. The $Fe_2P_2S_6$ is constructed by neutral $[Fe_2P_2S_6]$ slabs, which are constructed by $[FeS_6]$ octahedron and $[P_2S_6]$ motifs. Within the asymmetric unit cell of $Fe_2P_2S_6$, there are two independent Fe atomic positions. With leaving one Fe atomic position vacant and replacing another Fe atomic position by In atoms, the neutral $[Fe_2P_2S_6]$ slabs were changed to $[InP_2S_6]^-$ slabs. The P-P homoatomic bonds are broken with incorporation of In atoms, which results in the oxidation states for P changing from 4+ to 5+. One additional sulfur atom is incorporated in to $[InP_2S_6]^-$ slabs to link $[PS_4]$ tetrahedra, which forms $[InP_2S_7]^-$ slabs. Please notice, each $[InS_6]$ octahedral was shifted along [010] direction about $\frac{1}{4}$ b distance. The negatively charged $[InP_2S_6]^-$ slabs are compensated by inserting K^+ cations. The trivalent In atoms within $KInP_2S_7$ can be replaced by isovalent transition metals such as Cr^{3+} and V^{3+}, which introduce potential magnetic application into this system.

3.3. Bonding Pictures of $KInP_2S_7$

The $AIIIP_2S_7$ (A = K, Rb, Cs; III = V, Cr, In) family crystallizes in acentric *C*2 (no. 5) space group. The basic building units for $KInP_2S_7$ are intrinsically distorted $[PS_4]$ tetrahedron and $[InS_6]$ octahedron. The P-S distances within $[PS_4]$ tetrahedra are 2.005–2.137 Å. The bonding picture studies shows the covalent bonding nature of P-S interactions (Figure 3a). There are obvious attractors located between the P and S atoms. The covalent P-S interactions exhibit strong bonding characters with −ICOHP of 5.738 eV/bond for 2.05 Å P-S interactions. (Figure 3b). The P-S interactions were revealed to play an important role for contributing to the optical properties of $KInP_2S_7$ (*vide infra*). The distorted $[InS_6]$ octahedron is shown in Figure 3c. The central In atom is surrounded by four In-S interactions of 2.58 Å and two elongated In-S interactions of 2.70 Å, namely a 4 + 2 coordination environment. The two elongated 2.70 Å In-S interactions are located at the axial position and equatorial position, respectively. The COHP calculation (Figure 3b) and ELF (Figure S2) calculation indicated strong ionic interaction nature of In-S interactions. The calculated –ICOHPs for 2.58 Å In-S interactions and 2.70 Å In-S interactions are 1.939 eV/bond and 1.355 eV/bond, respectively. The distorted $[InS_6]$ octahedron contribute less than that of distorted $[PS_4]$ tetrahedron to the total optical properties of $KInP_2S_7$ (*vide infra*).

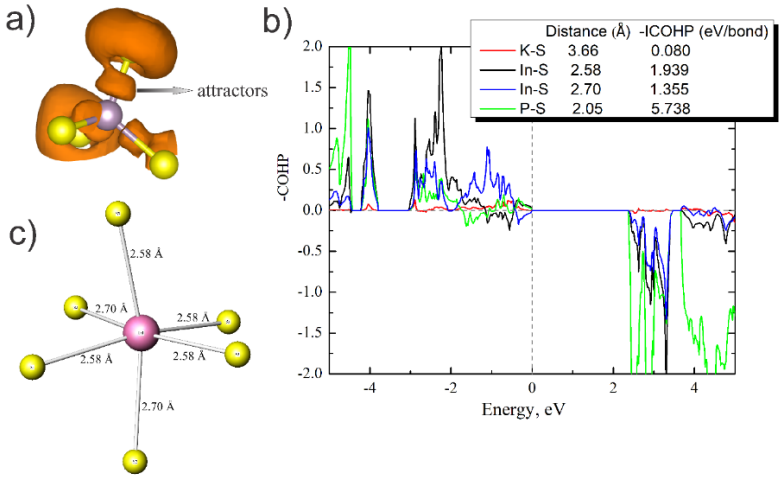

Figure 3. (**a**) 3D isosurfaces of the ELF for a $[PS_4]$ tetrahedral within $KInP_2S_7$ with η = 0.75, P: gray, S: yellow. (**b**) COHP analyses of selected interactions within $KInP_2S_7$. (**c**) The $[InS_6]$ octahedron with bond distances labeled. P: gray, In: pink, S: yellow.

3.4. Magnetic Properties of $KCrP_2S_7$

The layered crystal structure coupled with flexible chemical properties of the $AIIIP_2S_7$ (A = K, Rb, Cs; III = V, Cr, In) family indicate the potential broad applications such as magnetic properties and optical applications and the interface between them. Hence, we measured the magnetic properties of high quality $KCrP_2S_7$ crystals (Figure 1 inset). Figure 4a shows the zero-field cooling (ZFC) and field cooling (FC) temperature dependene of the magnetic susceptibility of a $KCrP_2S_7$ single crystal measured under a magnetic field of 1 T employed within the ab plane. A clear peak is observed at 21 K, which should be attribute to an antiferromagnetic transition because of the overlaping of the ZFC and FC data and a neagtive Weiss temperature of −50 K from fitting the data to the modied Curie-Weiss law (Figure 4a). The antiferromagnetic state is also consistent with the linear field dependence in the low field region of the isothermal magnetization, as shown in Figure 4b. At T = 2 K, a metamagnetic spin-flop transtion is observed around 3 T, which is suppressed up on increasing temeprature and disappears above the magnetic ordering temeprature (Figure 4b). Such spin-flop transition is not observed under an out-of-plane magnetic field. (Figure 4b, inset). These observations agree well with the antiferromagnetic ground state with an inplane easy axis of the Cr^{3+} moment. Similar scenario has also been observed in other layered magnetic materials such as $NiPS_3$ [55]. The effective magnetic moment μ_{eff} estimated from the Curie constant of the fits are 3.80 μ_B, which agrees well with the theoretical values of trivalent Cr^{3+} (3.87 μ_B). A previous study of $KCrP_2S_7$ crystals grown by KBr also found an antiferromagnetic transition at 17 K [37]. The calculated μ_{eff} with employing H//c* is 3.95 μ_B [37]. In this work, high quality crystals were grown by solid state chemistry method, which eliminated the possibility of incorporation of foreign elements. The trivalent M^{3+} is also supported by the electron-precise nature of $KInP_2S_7$, where In is also trivalent (*vide infra*).

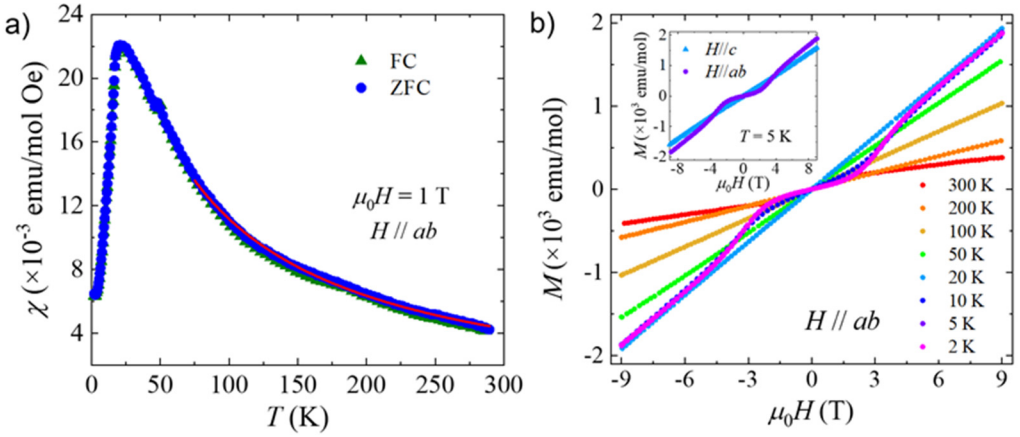

Figure 4. (**a**) Temperature dependence of dc magnetic susceptibility of selected $KCrP_2S_7$ crystals measured in a field of 1 T employed parallel to the ab plane (*H//ab*). The red solid lines indicate the fit to the modified Curie-Weiss law. (**b**) Field dependence of isothermal magnetization (M) of $KCrP_2S_7$ at different temperatures, measured under *H//ab*. Inset: isothermal magnetization at 5 K with both in-plane (*H//ab*) and out-of-plane magnetic fields.

3.5. Electronic Structures of $KInP_2S_7$

Since the trivalent nature of III metals are within the $AIIIP_2S_7$ (A = K, Rb, Cs; III = V, Cr, In) family, the charge-balanced formula $(A^+)(III^{3+})(P^{5+})_2(S^{2-})_7$ can be established by assigning a formal charge of 1+ to the alkali metals, 5+ to the P atoms, and 2− to the sulfur atoms. The charge-balanced nature of $KInP_2S_7$ was verified by TB-LMTO-ASA calculations (Figure 5) and UV-Vis measurements (*vide infra*). $KInP_2S_7$ is predicated to be an indirect bandgap semiconductor with the top of valance band and the bottom of conduction band located at the *A* points and the Λ points, respectively. The energy gap separating the conduction band and the valence band is 2.38 eV, which is comparable to

the experimentally measured value of 2.4(1) eV (*vide infra*). The top of the valance band is mainly contributed by S 3p orbitals (Figure 5b) together with very small contribution from the In 5s and 5p orbitals. There is no accountable contribution from P 3p orbitals and K 4s orbitals at the bottom of the top of valence band. The S 3p orbitals and the P 3p orbitals significantly contribute to the bottom of the conduction band, where very small amounts are contributed are from the In 5s and 5p orbitals and K 4s orbitals. Hence, we can anticipate that the optical properties of $KInP_2S_7$ are mainly contributed by [PS_4] tetrahedra units coupled with certain contribution from the [InS_6] octahedra.

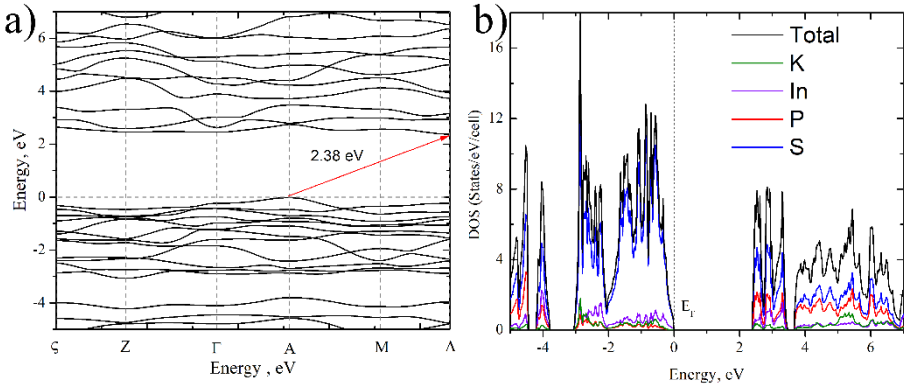

Figure 5. (**a**) Calculated band structure and (**b**) DOS of $KInP_2S_7$.

3.6. Linear and Nonlinear Optical Properties of $KInP_2S_7$

$KCrP_2S_7$ is estimated to have a very small bandgap with the black appearance of the crystals. Hence, the optical properties were mainly carried on $KInP_2S_7$. The bandgap of $KInP_2S_7$ was estimated by UV-Vis measurements. The experimentally measured value is 2.4(1) eV (Figures S3 and S4), which agrees well with our theory study of 2.38 eV. $KInP_2S_7$ was predicated by L. Kang et al. to possess moderate SHG effects (18 × KDP) [2]. Our experiments verified this predication as shown in Figure S5. $KInP_2S_7$ does not exhibit type-I phase-matching behavior, where the SHG intensity increases first then decreases with particle size increasing. For $KInP_2S_7$ sample of particle size of 100 μm, the SHG intensity of $KInP_2S_7$ is about 0.51 × $AgGaS_2$. Notice that, the quality of crystals may affect the SHG response [45]. $KInP_2S_7$ exhibited impressively high LDT of 5.2 × $AgGaS_2$ (Table S1), which may originate from its high bandgap. More study is required to understand the high LDT of $KInP_2S_7$., The optical properties of $KInP_2S_7$ are dominantly contributed by [PS_4] tetrahedra. Hence, a future bandgap engineering possibility is to modify the [PS_4] tetrahedron, in example, by introducing As atoms or Sb atoms to replace P atoms so to suppress the bandgap and enhance SHG response [56]. To further understand the optical properties of $KInP_2P_7$, a DFT calculation is undergoing [57–59].

4. Conclusions

Two structurally known thiophosphates, $KInP_2S_7$ and $KCrP_2S_7$, were revisited in this work. Single phases and crystals of $KInP_2S_7$ and $KCrP_2S_7$ were grown by high temperature solid state reactions. $KCrP_2S_7$ is isostructural to $KInP_2S_7$, which features a layered structure. $KInP_2S_7$ and $KCrP_2S_7$ possess a close relationship to the layered thiophosphate $M_2P_2S_6$, where the divalent metals within $M_2P_2S_6$ are replaced by In^{3+} or Cr^{3+} and break down the P-P interactions. The K cations were inserted between $[MP_2S_7]^-$ $_{M = Cr\ or\ In}$ to compensate the charge and fill the space. Magnetic measurement on mm-sized crystals of $KCrP_2S_7$ verified the antiferromagnetic transition around 21K and the trivalent nature of Cr atoms. The bonding pictures of $KInP_2S_7$ were studied by ELF coupled with COHP calculations. The intrinsically distorted [PS_4] tetrahedra and [InS_6] octahedra are made by strong covalent P-S interactions and ionic In-S interactions, respectively. $KInP_2S_7$ is predicated to be an indirect bandgap semiconductor of 2.38 eV, which is confirmed by the UV-Vis measurement of 2.4(1) eV. Electronic structure analysis confirmed that the main contributing factor to

the optical properties of $KInP_2S_7$ are $[PS_4]$ tetrahedra while small amounts of contribution are from $[InS_6]$ octahedra. $KInP_2S_7$ is not a type-I phase-matching materials and exhibits moderate SHG response (0.51 × $AgGaS_2$, sample of particle size of 100 μm). The LDT of $KInP_2S_7$ is very high at 5.2 × $AgGaS_2$. Bandgap engineering were undergone to enhance the SHG response of $KInP_2S_7$.

Supplementary Materials: The following supporting information can be downloaded at: https://www.mdpi.com/article/10.3390/cryst12111505/s1, Room temperature powder X-ray diffraction data (Figure S1), ELF calculation (Figure S2), UV-Vis data (Figure S3), Tauc plots (Figure S4), SHG measurements (Figure S5), LDT measurement results (Table S1).

Author Contributions: C.C. and V.N.: Methodology, Validation; S.K.C. and J.H.: Resources and Investigation; S.G.: Resources; J.W.: Data curation, Formal analysis, Funding acquisition, Supervision, Writing—original draft, Writing—review and editing. All authors have read and agreed to the published version of the manuscript.

Funding: This research was funded by NASA's support and award number No. 80NSSC22M0028. Work at the University of Arkansas (magnetic property study) is supported by the U.S. Department of Energy, Office of Science, Basic Energy Sciences program under Grant No. DE-SC0022006.

Institutional Review Board Statement: Not applicable.

Informed Consent Statement: Not applicable.

Data Availability Statement: Not applicable.

Acknowledgments: J.W. would like to thank Kui Wu at Hebei University for helping on LDT measurement.

Conflicts of Interest: The authors declare no conflict of interest.

References

1. Li, Z.; Jiang, X.; Zhou, M.; Guo, Y.; Luo, X.; Wu, Y.; Lin, Z.; Yao, J. $Zn_3P_2S_8$: A Promising Infrared Nonlinear-Optical Material with Excellent Overall Properties. *Inorg. Chem.* **2018**, *57*, 10503–10506. [CrossRef] [PubMed]
2. Kang, L.; Zhou, M.; Yao, J.; Lin, Z.; Wu, Y.; Chen, C. Metal Thiophosphates with Good Mid-Infrared Nonlinear Optical Performances: A First-Principles Prediction and Analysis. *J. Am. Chem. Soc.* **2015**, *137*, 13049–13059. [CrossRef] [PubMed]
3. Anema, A.; Grabar, A.; Rasing, T. The Nonlinear Optical Properties of $Sn_2P_2S_6$. *Ferroelectrics* **1996**, *183*, 181–183. [CrossRef]
4. Hu, Q.; Ruan, K.; Wang, Y.; Ding, K.; Xu, Y. Synthesis and Nonlinear Optical Properties of New Gallium Thiophosphate $Rb_2Ga_2P_2S_9$. *New J. Chem.* **2019**, *43*, 12468–12474. [CrossRef]
5. Chen, M.-M.; Zhou, S.-H.; Wei, W.; Ran, M.-Y.; Li, B.; Wu, X.-T.; Lin, H.; Zhu, Q.-L. $RbBiP_2S_6$: A Promising IR Nonlinear Optical Material with a Giant Second-Harmonic Generation Response Designed by Aliovalent Substitution. *ACS Mater. Lett.* **2022**, *4*, 1264–1269. [CrossRef]
6. Fan, Y.-H.; Jiang, X.-M.; Liu, B.-W.; Li, S.-F.; Guo, W.-H.; Zeng, H.-Y.; Guo, G.-C.; Huang, J.-S. Phase Transition and Second Harmonic Generation in Thiophosphates $Ag_2Cd(P_2S_6)$ and $AgCd_3(PS_4)S_2$ Containing Two Second-Order Jahn-Teller Distorted Cations. *Inorg. Chem.* **2017**, *56*, 114–124. [CrossRef]
7. Li, Z.; Zhang, S.; Huang, Z.; Zhao, L.-D.; Uykur, E.; Xing, W.; Lin, Z.; Yao, J.; Wu, Y. Molecular Construction from $AgGaS_2$ to $CuZnPS_4$: Defect-Induced Second Harmonic Generation Enhancement and Cosubstitution-Driven Band Gap Enlargement. *Chem. Mater.* **2020**, *32*, 3288–3296. [CrossRef]
8. Li, Z.; Zhang, S.; Xing, W.; Guo, Y.; Li, C.; Lin, Z.; Yao, J.; Wu, Y. Mixed-Metal Thiophosphate $CuCd_3PS_6$: An Infrared Nonlinear Optical Material Activated by Its Three-in-One Tetrahedra-Stacking Architecture. *J. Mater. Chem. C* **2020**, *8*, 5020–5024. [CrossRef]
9. Zhou, M.; Kang, L.; Yao, J.; Lin, Z.; Wu, Y.; Chen, C. Midinfrared Nonlinear Optical Thiophosphates from $LiZnPS_4$ to $AgZnPS_4$: A Combined Experimental and Theoretical Study. *Inorg. Chem.* **2016**, *55*, 3724–3726. [CrossRef]
10. Feng, J.; Hu, C.-L.; Li, B.; Mao, J.-G. $LiGa_2PS_6$ and $LiCd_3PS_6$: Molecular Designs of Two New Mid-Infrared Nonlinear Optical Materials. *Chem. Mater.* **2018**, *30*, 3901–3908. [CrossRef]
11. Li, M.-Y.; Ma, Z.; Li, B.; Wu, X.-T.; Lin, H.; Zhu, Q.-L. $HgCuPS_4$: An Exceptional Infrared Nonlinear Optical Material with Defect Diamond-like Structure. *Chem. Mater.* **2020**, *32*, 4331–4339. [CrossRef]
12. Chu, Y.; Wang, P.; Zeng, H.; Cheng, S.; Su, X.; Yang, Z.; Li, J.; Pan, S. $Hg_3P_2S_8$: A New Promising Infrared Nonlinear Optical Material with a Large Second-Harmonic Generation and a High Laser-Induced Damage Threshold. *Chem. Mater.* **2021**, *33*, 6514–6521. [CrossRef]

13. Huang, X.; Yang, S.-H.; Li, X.-H.; Liu, W.; Guo, S.-P. Eu2P2S6: The First Rare-Earth Chalcogenophosphate Exhibiting Large Second-Harmonic Generation Response and High Laser-Induced Damage Threshold. *Angew. Chem. Int. Ed.* **2022**, *61*, e202206791. [CrossRef] [PubMed]
14. Feng, J.-H.; Hu, C.-L.; Xu, X.; Li, B.-X.; Zhang, M.-J.; Mao, J.-G. $AgGa_2PS_6$: A New Mid-Infrared Nonlinear Optical Material with a High Laser Damage Threshold and a Large Second Harmonic Generation Response. *Chem.-Eur. J.* **2017**, *23*, 10978–10982. [CrossRef] [PubMed]
15. Ji, B.; Sarkar, A.; Wu, K.; Swindle, A.; Wang, J. A2P2S6 (A = Ba and Pb): A Good Platform to Study the Polymorph Effect and Lone Pair Effect to Form an Acentric Structure. *Dalton Trans.* **2022**, *51*, 4522–4531. [CrossRef]
16. Liu, B.-W.; Zeng, H.-Y.; Jiang, X.-M.; Wang, G.-E.; Li, S.-F.; Xu, L.; Guo, G.-C. $[A_3X]$ $[Ga_3PS_8]$ (A = K, Rb; X = Cl, Br): Promising IR Non-Linear Optical Materials Exhibiting Concurrently Strong Second-Harmonic Generation and High Laser Induced Damage Thresholds. *Chem. Sci.* **2016**, *7*, 6273–6277. [CrossRef]
17. Krauskopf, T.; Culver, S.P.; Zeier, W.G. Local Tetragonal Structure of the Cubic Superionic Conductor Na_3PS_4. *Inorg. Chem.* **2018**, *57*, 4739–4744. [CrossRef]
18. Krauskopf, T.; Culver, S.P.; Zeier, W.G. Bottleneck of Diffusion and Inductive Effects in $Li_{10}Ge_{1-x}Sn_xP_2S_{12}$. *Chem. Mater.* **2018**, *30*, 1791–1798. [CrossRef]
19. Duchardt, M.; Neuberger, S.; Ruschewitz, U.; Krauskopf, T.; Zeier, W.G.; der Günne, J.S.A.; Adams, S.; Roling, B.; Dehnen, S. Superion Conductor $Na_{11.1}Sn_{2.1}P_{0.9}Se_{12}$: Lowering the Activation Barrier of Na^+ Conduction in Quaternary 1–4–5–6 Electrolytes. *Chem. Mater.* **2018**, *30*, 4134–4139. [CrossRef]
20. Kaup, K.; Lalère, F.; Huq, A.; Shyamsunder, A.; Adermann, T.; Hartmann, P.; Nazar, L.F. Correlation of Structure and Fast Ion Conductivity in the Solid Solution Series $Li_{1+2x}Zn_{1-X}PS_4$. *Chem. Mater.* **2018**, *30*, 592–596. [CrossRef]
21. Bernges, T.; Culver, S.P.; Minafra, N.; Koerver, R.; Zeier, W.G. Competing Structural Influences in the Li Superionic Conducting Argyrodites $Li_6PS_{5-x}Se_xBr$ ($0 \leq x \leq 1$) upon Se Substitution. *Inorg. Chem.* **2018**, *57*, 13920–13928. [CrossRef] [PubMed]
22. Duchardt, M.; Ruschewitz, U.; Adams, S.; Dehnen, S.; Roling, B. Vacancy-Controlled Na^+ Superion Conduction in $Na_{11}Sn_2PS_{12}$. *Angew. Chem.* **2018**, *130*, 1365–1369. [CrossRef]
23. Fan, Y.-H.; Zeng, H.-Y.; Jiang, X.-M.; Zhang, M.-J.; Liu, B.-W.; Guo, G.-C.; Huang, J.-S. Thiophosphates Containing Ag^+ and Lone-Pair Cations with Interchiral Double Helix Show Both Ionic Conductivity and Phase Transition. *Inorg. Chem.* **2017**, *56*, 962–973. [CrossRef] [PubMed]
24. Dietrich, C.; Weber, D.A.; Culver, S.; Senyshyn, A.; Sedlmaier, S.J.; Indris, S.; Janek, J.; Zeier, W.G. Synthesis, Structural Characterization, and Lithium Ion Conductivity of the Lithium Thiophosphate $Li_2P_2S_6$. *Inorg. Chem.* **2017**, *56*, 6681–6687. [CrossRef]
25. Kraft, M.A.; Culver, S.P.; Calderon, M.; Böcher, F.; Krauskopf, T.; Senyshyn, A.; Dietrich, C.; Zevalkink, A.; Janek, J.; Zeier, W.G. Influence of Lattice Polarizability on the Ionic Conductivity in the Lithium Superionic Argyrodites Li_6PS_5X (X = Cl, Br, I). *J. Am. Chem. Soc.* **2017**, *139*, 10909–10918. [CrossRef]
26. Sun, Y.; Suzuki, K.; Hori, S.; Hirayama, M.; Kanno, R. Superionic Conductors: Li10þd $[Sn_ySi_{1-y}]$ 1þdP2À DS12 with a $Li_{10}GeP_2S_{12}$-Type Structure in the Li_3PS_4-Li_4SnS_4-Li_4SiS_4 Quasi-Ternary System. *Chem. Mater.* **2017**, *29*, 5858–5864. [CrossRef]
27. Wu, T.; Stone, M.L.; Shearer, M.J.; Stolt, M.J.; Guzei, I.A.; Hamers, R.J.; Lu, R.; Deng, K.; Jin, S.; Schmidt, J.R. Crystallographic Facet Dependence of the Hydrogen Evolution Reaction on CoPS: Theory and Experiments. *ACS Catal.* **2018**, *8*, 1143–1152. [CrossRef]
28. Zhang, X.; Luo, Z.; Yu, P.; Cai, Y.; Du, Y.; Wu, D.; Gao, S.; Tan, C.; Li, Z.; Ren, M.; et al. Lithiation-Induced Amorphization of Pd_3P_2S8 for Highly Efficient Hydrogen Evolution. *Nat. Catal.* **2018**, *1*, 460–468. [CrossRef]
29. Itthibenchapong, V.; Kokenyesi, R.S.; Ritenour, A.J.; Zakharov, L.N.; Boettcher, S.W.; Wager, J.F.; Keszler, D.A. Earth-Abundant Cu-Based Chalcogenide Semiconductors as Photovoltaic Absorbers. *J. Mater. Chem. C* **2012**, *1*, 657–662. [CrossRef]
30. Neuberger, S.; Culver, S.P.; Eckert, H.; Zeier, W.G.; Schmedt auf der Günne, J. Refinement of the crystal structure of $Li_4P_2S_6$ using NMR crystallography. *Dalton Trans.* **2018**, *47*, 11691–11695. [CrossRef]
31. Cheng, M.; Lee, Y.-S.; dos Reis, R.; Iyer, A.; Chica, D.; Kanatzidis, M.; Dravid, V. Structural and Chemical Analysis of Mixed Cation Antiferromagnetic Layered Metal Chalcophosphate $FeCoP_2S_6$. *Microsc. Microanal.* **2021**, *27*, 140–143. [CrossRef]
32. Usman, M.; Smith, M.D.; Klepov, V.V.; zur Loye, H.-C. One-Dimensional Quaternary and Penternary Alkali Rare Earth Thiophosphates Obtained via Alkali Halide Flux Crystal Growth. *Cryst. Growth Des.* **2019**, *19*, 5648–5657. [CrossRef]
33. Korotkov, A.S. Dependence of the Appearance of Crystal Acentricity on the Chemical Composition of Complex Inorganic Compounds and the Prediction of New Thiosilicates and Thiophosphates. *J. Electron. Mater.* **2020**, *49*, 4882–4891. [CrossRef]
34. Gutzmann, A.; Näther, C.; Bensch, W. $CsVP_2S_7$. *Acta Crystallogr. Sect. E Struct. Rep. Online* **2005**, *61*, i6–i8. [CrossRef]
35. Kopnin, E.; Coste, S.; Jobic, S.; Evain, M.; Brec, R. Synthesis and Crystal Structure Determination of Three Layered-Type Thiophosphate Compounds KMP_2S_7 (M = Cr, V, In). *Mater. Res. Bull.* **2000**, *35*, 1401–1410. [CrossRef]
36. Kim, K.; Na, J.; Yun, H. The Two-Dimensional Thiophosphate $CsCrP_2S_7$. *Acta Crystallogr. Sect. E Struct. Rep. Online* **2010**, *66*, i65. [CrossRef] [PubMed]
37. Sekizawa, K.; Sashida, M.; Takano, Y.; Takahashi, Y.; Takase, K. Magnetic Properties and Specific Heat of $KV_{1-x}Cr_xP_2S_7$. *J. Magn. Magn. Mater.* **2004**, *272–276*, E597–E598. [CrossRef]
38. Kurtz, S.K.; Perry, T.T. A Powder Technique for the Evaluation of Nonlinear Optical Materials. *J. Appl. Phys.* **1968**, *39*, 3798–3813. [CrossRef]

39. Tank, R.; Jepsen, O.; Burkhardt, A.; Andersen, O.K. *The Program TB-LMTO-ASA*, Version 4.7; Max-Planck-Institut für Festkörperforschung: Stuttgart, Germany, 1999.
40. Von Barth, U.; Hedin, L. A Local Exchange-Correlation Potential for the Spin Polarized Case. i. *J. Phys. C Solid State Phys.* **1972**, *5*, 1629–1642. [CrossRef]
41. Nguyen, V.; Ji, B.; Wu, K.; Zhang, B.; Wang, J. Unprecedented Mid-Infrared Nonlinear Optical Materials Achieved by Crystal Structure Engineering, a Case Study of (KX)P_2S_6 (X = Sb, Bi, Ba). *Chem. Sci.* **2022**, *13*, 2640–2648. [CrossRef]
42. Manriquez, V.; Galdámez, A.; León, D.R.; Garland, M.T. Crystal structure of potassium antimony hexathiodiphosphate, $KSbP_2S_6$. *Z. Für Krist.-New Cryst. Struct.* **2003**, *218*, 435–436. [CrossRef]
43. Manriquez, V.; Galdámez, A.; León, D.R.; Garland, M.T.; Jiménez, M. Crystal structure of potassium bismuth hexathiodiphosphate, $KBiP_2S_6$. *Z. Für Krist.-New Cryst. Struct.* **2003**, *218*, 151–252. [CrossRef]
44. Ji, B.; Guderjahn, E.; Wu, K.; Syed, T.H.; Wei, W.; Zhang, B.; Wang, J. Revisiting Thiophosphate $Pb_3P_2S_8$: A Multifunctional Material Combining a Nonlinear Optical Response and Photocurrent Response. *Phys. Chem. Chem. Phys.* **2021**, *23*, 23696–23702. [CrossRef] [PubMed]
45. Klingen, W.; Eulenberger, G.; Hahn, H. Über Hexathio- und Hexaselenohypodiphosphate vom Typ $M_2^{II}P_2X_6$. *Naturwissenschaften* **1968**, *55*, 229–230. [CrossRef]
46. Jörgens, S.; Mewis, A. Die Kristallstrukturen von Hexachalcogeno-Hypodiphosphaten des Magnesiums und Zinks. *Z. Für Anorg. Allg. Chem.* **2004**, *630*, 51–57. [CrossRef]
47. Liu, Q.; Zhou, W.; Gao, C.; Hu, T.; Zhao, X. Synthesis and Second-Order Optical Nonlinearity of DAMS/Mn2P2S6 Intercalated Materials by Ion Exchange Method. *Chem. Phys. Lett.* **2009**, *477*, 388–391. [CrossRef]
48. Rao, R.R.; Raychaudhuri, A.K. Magnetic Studies of a Mixed Antiferromagnetic System $Fe_{1-x}Ni_xPS_3$. *J. Phys. Chem. Solids.* **1992**, *53*, 577–583. [CrossRef]
49. Klingen, W.; Eulenberger, G.; Hahn, H. Uber die Kristallstrukturen von $Fe_2P_2Se_6$ und $Fe_2P_2S_6$. Z. *Anorg. Allg. Chem.* **1973**, *401*, 97–112. [CrossRef]
50. Prouzet, E.; Ouvrard, G.; Brec, R. Structure Determination of $ZnPS_3$. *Mater. Res. Bull.* **1986**, *21*, 195–200. [CrossRef]
51. Klingen, W.; Eulenberger, G.; Hahn, H. Über Hexachalkogeno-hypodiphosphate vom Typ M2P2X6. *Naturwissenschaften* **1970**, *57*, 88. [CrossRef]
52. Becker, R.; Brockner, W.; Schäfer, H. Kristallstruktur Und Schwingungsspektren Des Di-Blei-Hexathiohypodiphosphates $Pb_2P_2S_6$/Crystal Structure and Vibrational Spectra of $Pb_2P_2S_6$. *Z. Für Nat. A* **1983**, *38*, 874–879. [CrossRef]
53. Lifshitz, E.; Francis, A.H. Magnetic Resonance and Electronic Spectroscopy of $M_2P_2S_6$ Intercalation Compounds. In *Chemical Physics of Intercalation*; NATO ASI Series; Legrand, A.P., Flandrois, S., Eds.; Springer: Boston, MA, USA, 1987; pp. 425–431. [CrossRef]
54. Bhowmick, A.; Bal, B.; Ganguly, S.; Bhattacharya, M.; Kundu, M.L. Investigation of the Layered Compound Fe0.5Cd0.5PS3. *J. Phys. Chem. Solids.* **1992**, *53*, 1279–1284. [CrossRef]
55. Basnet, R.; Wegner, A.; Pandey, K.; Storment, S.; Hu, J. Highly sensitive spin-flop transition in antiferromagnetic van der Waals material MPS3 (M = Ni and Mn). *Phys. Rev. Mater.* **2021**, *2021. 5*, 064413. [CrossRef]
56. Cicirello, G.; Wu, K.; Zhang, B.B.; Wang, J. Applying Band Gap Engineering to Tune the Linear Optical and Nonlinear Optical Properties of Noncentrosymmetric Chalcogenides $La_4Ge_3Se_xS_{12-x}$(x = 0, 2, 4, 6, 8, 10). *Inorg. Chem. Front.* **2021**, *8*, 4914–4923. [CrossRef]
57. Reshak, A.H.; Abbass, N.M.; Bila, J.; Johan, M.R.; Kityk, I. Noncentrosymmetric Sulfide Oxide MZnSO (M = Ca or Sr) with Strongly Polar Structure as Novel Nonlinear Crystals. *J. Phys. Chem. C.* **2019**, *123*, 27172–27180. [CrossRef]
58. Ji, B.; Pandey, K.; Harmer, C.P.; Wang, F.; Wu, K.; Hu, J.; Wang, J. Centrosymmetric or Noncentrosymmetric? Transition Metals Talking in $K_2TGe_3S_8$(T = Co, Fe). *Inorg. Chem.* **2021**, *60*, 10603–10613. [CrossRef]
59. Bardelli, S.; Ye, Z.; Wang, F.; Zhang, B.; Wang, J. Synthesis, Crystal and Electronic Structures, and Nonlinear Optical Properties of $Y_4Si_3S_{12}$. *Z. Anorg. Allg. Chem.* **2022**, *648*, e202100. [CrossRef]